Article

Unraveling the prominent role of the Rh/ZrO-interface in the water-gas shift reaction via a first principles microkinetic study

Minttu Maria Kauppinen, Marko Melander, Andrey S Bazhenov, and Karoliina Honkala

ACS Catal., **Just Accepted Manuscript** • DOI: 10.1021/acscatal.8b02596 • Publication Date (Web): 29 Oct 2018

Unraveling the prominent role of the Rh/ZrO_2-interface in the water-gas shift reaction via a first principles microkinetic study

Minttu M. Kauppinen, Marko M. Melander, Andrey S. Bazhenov, and Karoliina Honkala*

Nanoscience Center, P.O. Box 35 (YN) FI-40014, Department of Chemistry, University of Jyväskylä, Finland

E-mail: karoliina.honkala@jyu.fi

Abstract

The industrially important water–gas shift (WGS) reaction is a complex network of competing elementary reactions, where the catalyst is a multicomponent system consisting of distinct domains. Herein we have combined density functional theory calculations with microkinetic modeling to explore the active phase, kinetics, and reaction mechanism of the WGS over Rh/ZrO_2. We have explicitly considered the support, metal, and their interface and find that the Rh/ZrO_2 interface is far more active towards WGS than Rh(111) facets, which are susceptible to CO poisoning. CO_2 forming on the zirconia support rapidly transforms into formate. These findings demonstrate the central role of the interface in the water–gas shift reaction, and the importance of modeling both the support and the metal in bifunctional systems.

Keywords

water-gas shift, heterogeneous catalysis, density functional theory, microkinetics, bifunctional, metal-support interface

Introduction

Water–gas shift (WGS) reaction converts water and carbon monoxide to hydrogen and carbon dioxide,[1] and presents a key reaction in many industrial processes including e.g., steam reforming,[2–4] methanation,[5] and Fischer-Tropsch reactions.[6] A number of different metal-oxide combinations are known to catalyze the WGS reaction, with varying activity, such as Au/MgO[7–9], Pt/CeO_2[7,10,11], Pt/TiO_2[7,11] and Cu/CeO_2[7] to name but a few. Experimental studies highlight the bifunctionality of WGS catalysts, where both active metal component and support oxide contribute to the reaction mechanism, and thus to overall activity.[12,13] In particular, the support can have a major effect, as in the case of platinum promoted WGS catalysts, where the order of activity for different supports has been reported as Pt/TiO_2 >$Pt/CeO_2/Al_2O_3$ >Pt/ZrO_2 ≥Pt/CeO_2 >Pt/Fe_2O_3.[7] The ordering of catalysts based on activity is challenging, since also the reaction conditions and preparation method have an effect, making it difficult to compare results obtained in different studies.

The metal-oxide interface has been computationally and experimentally identified as a potential active site for WGS on a multitude of bifunctional catalytic systems,[8,9,14–21] where the reaction mechanism depends on the chemical nature of the metal and support together with reaction conditions.[1] One less studied material, zirconia supported rhodium, has been previously demonstrated to be active for the WGS,[7,22] but little is known about the exact reaction mechanism and the identity of the active site. It is a promising material, as both zirconia[23] and Rh/ZrO_2[24] are known to have excellent thermal stability, and Rh/ZrO_2 has been recently shown to be resistant to the sintering of the Rh nanoparticles.[25] Recently, the material has also gained interest as a catalyst for partial oxidation of methane.[26] A

simple five step Langmuir-Hinshelwood kinetic model has been previously used to represent experimental data on the WGS over a Rh/ZrO_2 catalyst.[27] The model does not make assumptions about the possible intermediates of the surface reaction steps, although hydroxyl was suggested to be one of the important reaction intermediates in an earlier study.[22] In that study, the Mars-van-Krevelen type redox mechanism was ruled out based on the observation that rhodium was in a metallic form under WGS reaction conditions. Hydroxyl, carbonates, and carboxylate were suggested to be possible reaction intermediates, while formates were observed on the zirconia support of the catalyst at temperatures below 623 K[22].

In general, multiple reaction mechanisms have been put forward for the water–gas shift reaction on oxide supported metal catalysts, and the dominant mechanism depends on both the nature of the catalyst and the support. It is commonly suggested that WGS prefers the so-called "redox" mechanism over reducible oxide supports.[1,28,29] In this Mars-van-Krevelen-type mechanism the oxide support provides lattice oxygen for the oxidation of CO into CO_2 leaving an oxygen vacancy behind. The oxide is subsequently reoxidized by water which dissociates into the oxygen vacancy producing hydrogen in the process. Irreducible oxides, such as zirconia,[30] are thought to be incapable of providing lattice oxygens for the redox reaction, and therefore alternative "associative" mechanisms have been put forward for catalysts supported on those materials,[12,15] as well as for CeO_2 supported systems.[10,11] In associative pathways, CO reacts on the catalyst surface with dissociated water to produce an intermediate (e.g. carboxyl or formate) species which then dissociates into a hydrogen atom and CO_2. The nature of this intermediate has been under debate.[10,11,15,31–38] Several computational studies on different unsupported metal surfaces suggest that carboxyl is the reaction intermediate for the associative mechanism.[31–34] However, many experimental groups have observed formate on the oxide support under WGS reaction conditions and have argued it to be the main reaction intermediate.[10,11,35,37,38] Formate is said to be formed from the reaction between CO and a "terminal" OH group bound oxygen down to a single metal cation of the oxide, generating a bidentately bound formate.[11,15,36,38,39] The reaction is unlikely to occur

in a single low barrier step due to the many bonds that are required to be broken and formed simultaneously. In contrast, carboxyl can be formed in a single step from CO and OH.

Another pathway that also does not require the formation of oxygen vacancies on the support is the "surface redox" mechanism, in which water fully dissociates to form H_2 and atomic oxygen, which can then oxidize CO into CO_2.[40] Complete water dissociation can take place via two different pathways. After the initial partial dissociation of water into OH and H, atomic oxygen can be formed from direct dissociation of OH, or from disproportionation reaction between two OH groups to form H_2O and O. As the surface redox pathway does not require the reduction and oxidation of the oxide support, it can, in principle, operate on the metal alone, and has been included in many DFT studies on the WGS on unsupported metal surfaces.[31–33,41–43] Surface redox was originally thought to be the main reaction mechanism on the Cu(111) surface,[40] however it was later shown in a DFT study that WGS proceeds through a carboxyl mechanism on Cu(111) instead.[31] The surface redox route has been recently shown to be the dominant mechanism for Ni/Al_2O_3 in a combined computational and experimental study.[18]

Computational studies typically employ slab models to perform calculations for the WGS over metal catalysts,[31–33,41–43] however, since the slab contains only metal sites, the models completely ignore the possible role of the underlying oxide supports, and by extension, the catalyst-support interface. The forward and reverse WGS reactions over rhodium have also been previously studied employing slab models of the Rh(111)-facet.[33,42,44] These studies employed only DFT calculations, and no solid understanding was reached about the dominating mechanism for the WGS on Rh(111). The role of formate was only explicitly considered in Ref. [33], where it was stated that the formate pathway was energetically competitive with the redox and carboxyl pathways. That study suggests that formate is the most abundant experimentally observed intermediate because its formation barrier is lower than its dissociation barrier. Overall, the rationalization of obtained DFT results on WGS calls for further analysis, such as a microkinetic modeling, which allows resolving the dominant pathway

under varying reaction conditions. Furthermore, a catalyst model including both the metal and the support might be needed to better represent the material of interest.

While catalyst-support interfaces are in principle straightforward to model, constructing a computationally feasible model including necessary details is difficult. In cluster models, the metal catalyst consisting of up to several tens of atoms is placed on an oxide slab.[16,18,45–49] This can be a useful technique for modeling metal clusters and small particles, but is unsuitable for modeling nanoparticles in the range larger than e.g. 3 nm, active for WGS on Rh/ZrO_2.[22] Recently, computational studies have employed oxide supported metal nanorods to model the metal-oxide interface.[8,9,17,19,50–52] In these models, a $2-3$ layers thick metal nanorod is placed on an oxide surface slab. The calculations are periodic along the length of the rod, meaning the rod is infinitely long. This construction can be taken to represent an actual nanowire with a cross section of a few atoms, or the perimeter of an arbitrarily large nanoparticle.

First principles microkinetic modeling is often used to unravel the complex reaction network and relate the zero Kelvin and zero pressure DFT results to the real catalytic process taking place at reaction conditions.[4,53,54] For WGS reaction, there exists DFT based microkinetic models for unsupported metal surfaces,[31,32] but as explained above, those calculations exclude the potentially important contribution from the support. Recently, DFT based WGS microkinetic models have been constructed for oxide supported metal structures, namely Ni/Al_2O_3,[18] Au/TiO_2,[19], Cu/ZrO_2,[51] and Au/MgO.[8] All of these studies highlight the metal-oxide interface to be of significant importance to the WGS activity for the materials studied, information which would not be attainable without an explicit interface model. For the Ni_{55}/γ-Al_2O_3 cluster model, the surface redox reaction was shown to occur at the metal-support interface sites, with OH dissociation as the rate limiting step.[18] For the gold catalyst supported on the irreducible MgO, represented by a nanorod model, WGS was shown to proceed via the carboxyl mechanism.[8] The carboxyl formation step was found to be rate limiting. In contrast, when gold is supported on reducible TiO_2, WGS proceeds

through the Mars-van-Krevelen-type redox reaction with water dissociation as a rate limiting step, as demonstrated using a nanorod model for $Au/TiO_2(110)$.[19] Comparing the MgO and TiO_2 supported gold systems reveals how great an impact the choice of support has on the mechanism. A $Cu/m\text{-}ZrO_2(\bar{2}12)$ rod model was used to study the reactivity of copper nanowires supported on zirconia.[51] It was found that although the interfacial sites do not directly take part in the WGS mechanism, the ZrO_2 support facilitates the WGS by modifying the Cu sites in the immediate vicinity of the oxygen-rich interface. The reaction was found to occur through the carboxyl mechanism, with water dissociation as the rate limiting step. All of these studies highlight the fact that depending on the identity of the metal and support, the WGS can occur through vastly different reaction mechanisms, the promoting effect of the interface being complex and varied.

In this work, we undertake a multiscale computational study of WGS over *m*-zirconia supported rhodium nanoparticles to elucidate the reaction mechanism and to understand how different constituents of a catalyst, the support, "bulk" nanoparticle, and the catalyst/support-interface contribute to overall activity and what is the active phase of a catalyst. We use three model systems to capture the bifunctional nature of the Rh/ZrO_2 catalyst and include a complete set of elementary reaction steps to construct a WGS reaction network. We begin by presenting DFT results for the thermodynamic and kinetic properties of the reaction. With first principles microkinetic modeling, we analyze the reaction mechanism and the contribution of the components of the catalyst towards CO conversion. We close by comparing our findings to existing experimental observations and highlight the complexity of water–gas shift chemistry, the challenges in microkinetic modeling, and the importance of different sites and parts of a catalyst to form overall understanding of the reaction at hand.

Methods

Computational Details

All DFT calculations reported herein were performed using the GPAW 1.1.0 software.[55–58] The exchange and correlation effects were described within the generalized gradient approximation employing the Perdew-Burke-Ernzerhof (PBE) functional[59,60] and the core electrons of elements were treated with the PAW[61] setups with the frozen core approximation. The Brillouin zones for the rhodium and zirconia surfaces were sampled using a $(6 \times 6 \times 1)$ and a $(4 \times 4 \times 1)$ Monkhorst-Pack mesh of k-points, respectively, while the interface and the gas phase species were treated at the Γ-point.

The transition states (TS) were located using a climbing image automated nudged elastic band (CI-AutoNEB) method[62–65] or constraint optimization, and they were confirmed by the presence of a single imaginary vibrational mode along the reaction coordinate. For full list of imaginary frequencies, please refer to the supporting info (SI). The vibrational analysis was performed for the reaction intermediates on all three model systems in order to calculate zero-point energies (ZPE). In each case, the analysis was performed only for the adsorbate atoms, and frequencies less than 100 cm^{-1} in energy were omitted from the ZPE calculations. Reaction rates for surface reactions were computed using harmonic transition state theory.[66] For non-activated adsorption steps, the rates were calculated using kinetic gas theory (see SI). Entropy of adsorbed species was calculated using the harmonic approximation as implemented in ASE,[57] while gas-phase entropies were taken from the NIST database.[67]

We thoroughly screened possible adsorbate structures at the interface with the LCAO[68] DZP basis allowing them to relax until the maximum residual force was below 0.1 $eV \cdot Å^{-1}$. The most promising interface structures as well as rhodium and zirconia surfaces were then optimized in the grid basis with a 0.2 Å maximum grid spacing. In grid basis, the structures were allowed to relax until the maximum residual force was below 0.05 $eV \cdot Å^{-1}$.

The interface was modeled with a 40-atom Rh nanorod covalently bound to a 2ML-thick

m-$ZrO_2(\bar{1}11)$ surface with the Rh(111) facet of the front edge of the rod facing towards zirconia to mimic the perimeter of a large nanoparticle, please see Fig. 1c. The m-$ZrO_2(\bar{1}11)$ slab was chosen to represent the support since monoclinic zirconia is the most stable polymorph at typical WGS conditions,[69] and $(\bar{1}11)$ the most stable facet.[69–71] The size of the unit cell of the ZrO_2 slab was (2x2), which was chosen to minimize lattice mismatch between the oxide and the Rh-rod. For the size of the chosen unit cell, the lattice mismatch between bulk rhodium and m-$ZrO_2(\bar{1}11)$ is -1.0 % and 6.8 % along the axes a and b (see Figure 1c), respectively. Since the calculations have to be periodic along the length of the rod, the alignment where the lattice mismatch is smallest, -1.0 %, was chosen. This means that in the final interface model, the rhodium-rhodium bonds are compressed by 1.0 % along the length of the rod. To optimize the interface structure, the top ZrO_2 layer and the all the Rh atoms were allowed to relax freely, keeping the atoms in the bottom layer of the ZrO_2 slab fixed at their ideal bulk positions. Several starting structures with different positioning of the rod along the b-axis were optimized in the LCAO-DZP basis, and from those the lowest energy structure was chosen for further study. We also evaluated the strain and ligand induced change in the d-band center of the first row of Rh atoms as per the procedure described in Ref. 52. The change in the d-band center is -0.45 eV and 0.10 eV due to the ligand and strain effect, respectively, making the overall change in the d-band center modestly negative by -0.35 eV. The strain effect for the Rh/ZrO_2-interface is smaller in magnitude than in the case of the Rh/MgO-interface due to the smaller lattice mismatch.[52] We also observe a greater ligand effect as compared to the Rh/MgO-interface, making the overall change in the d-band center more negative in our case.[52]

To eliminate the interaction between an adsorbate and the back side of the next periodic image of the rod, adsorbates were only placed on oxide sites close to the Rh/ZrO_2 interface. On the rod, adsorbates were placed on the first row of Rh atoms. The most stable extended rhodium (111) surface (Fig.1a) was modeled with a (2×2) slab with a lattice constant of 3.857 Å. The slab was four atomic layers thick and the two bottom most layers were kept

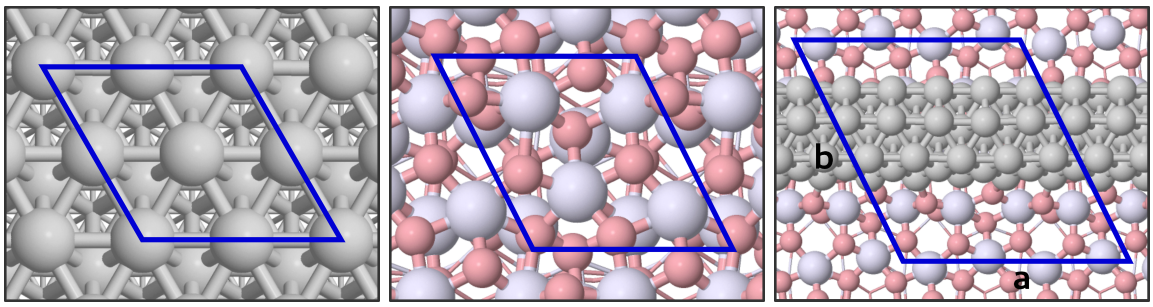

(a) Rh(111) (b) m-$ZrO_2(\bar{1}11)$ (c) Interface

Figure 1: Models used for the three studied systems: a Rh(111) surface, a $ZrO_2(\bar{1}11)$ surface, and a $Rh/ZrO_2(\bar{1}11)$ interface . Rh, Zr and O atoms are shown in grey, lavender, and pink, respectively. The unit cell of the periodic structure is indicated with indigo outlines.

fixed. The zirconia terrace was modeled with a m-$ZrO_2(\bar{1}11)$ (1×1) 2D slab (Fig. 1b) which was four stoichiometric ZrO_2 layers thick with the two bottom most layers fixed at their ideal bulk positions. The model is described in detail in our previous work.[70] Gas phase H_2O, H_2, CO, and CO_2 molecules were calculated in a non-periodic computational cell that was $12 \times 12 \times 12$ Å in size with 0.2 Å maximum grid spacing.

Microkinetic Model

In a microkinetic model the pressure and surface coverage of each species as a function of time is obtained by solving the reaction rate equations. Rate constants are based on DFT-computed activation free energies and pre-factors are taken to be equal to $\frac{k_b T}{h}$. The complete reaction network and details of the microkinetic model are given in the SI. For brief, we used an in-house code to solve the reaction rate equations for a continuous stirred tank reactor. We solve the dynamical equations explicitly as a function of time because this gives important information on the transient time dependent dynamics of the complex system. Furthermore, this approach provides information on the reaction mechanism and how different species react, form, and disappear with time. The simulation time was set to 10000 s for all runs to ensure that the system had enough time to reach dynamic steady state. Catalyst mass, BET, Rh loading, and particle diameter were set at 100 mg, 100 cm^2/g,

0.5 wt.%, and 5 nm, respectively, to mimic experimental values. For analyzing the results, we performed rate control analyses (for more details see SI).[72] From the time-dependent fluxes for ($\dot{n}_i(t)$) reactants and products, we calculated the conversion as

$$X_{prod}(t) = \frac{\int_t dt \dot{n}^{out}_{prod}(t)}{\int_t dt \dot{n}^{in}_{reac}(t)} \approx \frac{\dot{n}^{out}_{prod}(t)}{\dot{n}^{in}_{reac}(t)} = \frac{P_{prod}(t)}{P^{in}_{prod}(t)} = X^{SS}_{prod} \quad (1)$$

where *in* and *out* refer to in-put and out-put feeds while P is the pressure. We approximate the full conversion to be the time-independent steady-state (SS) conversion X^{SS}. Reaction order with respect to the reactant and product gases was also determined by varying the partial pressure of one gas while keeping the others constant. For full details please see SI.

Results

We start with by presenting DFT results for a WGS reaction thermodynamics and kinetics over three different components of a Rh/ZrO_2 catalyst. Then we analyze and compare the DFT-computed reaction mechanisms collectively. Finally, we report predicted CO conversions and surface coverages from the microkinetic analysis.

Results from DFT calculations

We have considered the three most commonly proposed reaction pathways for the WGS: Associative carboxyl route, associative formate route, and the redox route. Table 1 summarizes the corresponding elementary steps. Both reaction themodyamics and kinetics of the elementary steps were evaluated on all three model systems. In the following sections, we analyze the elementary steps for these pathways addressing both adsorption and transition state geometries as well as their zero-point corrected reaction energies and activation barrier.

Table 1: Labeled elementary steps in the reaction network for the WGS. * denotes a general empty adsorption site.

Label	Reaction
R1	$H_2O + * \rightleftharpoons H_2O^*$
R2	$H_2O^* + * \rightleftharpoons OH^* + H^*$
R3	$OH^* + * \rightleftharpoons O^* + H^*$
R4	$OH^* + OH^* \rightleftharpoons O^* + H_2O^*$
R5	$H^* + H^* \rightleftharpoons H_2(g) + 2*$
R6	$CO(g) + * \rightleftharpoons CO^*$
R7	$CO^* + O^* \rightleftharpoons CO_2^* + *$
R8	$CO_2^* \rightleftharpoons CO_2(g) + *$
R9	$OH^* + CO^* \rightleftharpoons COOH^* + *$
R10	$COOH^* + * \rightleftharpoons CO_2^* + H^*$
R11	$CO^* + H^* \rightleftharpoons HCO^* + *$
R12	$HCO^* + O^* \rightleftharpoons HCOO^{**}$
R13	$HCOO^{**} \rightleftharpoons CO_2^* + H^*$

Water Dissociation and Disproportionation

Regardless of the overall reaction mechanism, the WGS reaction always begins with at least partial water dissociation leading to the formation of hydrogen and a hydroxyl species followed by either a reaction with CO or a complete water dissociation to atomic hydrogen and oxygen. Figure 2 summarizes the potential energy surface (PES) for partial and complete water dissociation over the three model systems discussed in detail below. On ZrO_2, molecular water adsorbs preferably on a Zr cation via its oxygen atom with strongly exothermic adsorption energy of −0.96 eV. At the interface, adsorption energy is less exothermic being −0.74 eV and water again binds on top of a Zr cation with the hydrogens pointing towards the Rh rod. The weakest adsorption energy for a single water molecule is found on Rh(111), where water also favors top site adsorption but has a substantially less exothermic adsorption energy of −0.32 eV. The Rh(111) surface presents the highest activation energy for water dissociation and the computed barrier for O–H cleavage is 0.72 eV with the O–H bond length 1.54 Å at the transition state. Overall, the reaction is mildly endothermic by +0.09 eV. Although the desorption barrier for H_2O is lower than the barrier for partial dissociation, the situation might change dramatically with increasing water coverage, since water molecules

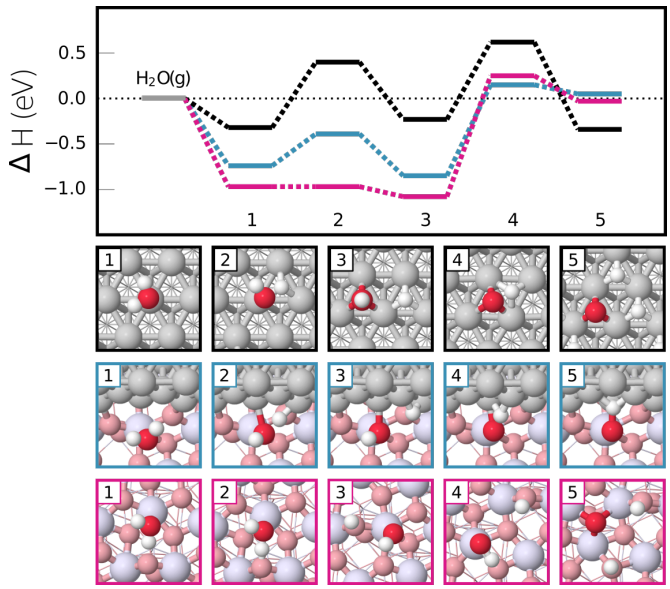

Figure 2: Potential energy diagram and adsorption structures for water adsorption and dissociation on Rh, ZrO_2, and the Rh/ZrO_2-interface shown in black, pink, and teal lines, respectively. Rh, Zr, H, O_{ads} and O_{lat} atoms are shown in grey, lavender, white, red, and pink, respectively.

form intermolecular hydrogen bonds stabilizing the adsorption.[73,74] Our findings for Rh(111) agree well with the previous DFT results for water adsorption and activation on Rh(111).[75] In contrast to Rh(111), we find that on m-$ZrO_2(\bar{1}11)$ water dissociation is spontaneous and slightly exothermic with the reaction energy of −0.10 eV. This agrees with the experimental observation that water adsorbs dissociatively on m-ZrO_2,[71] as well as previous DFT calculations for the thermodynamics of water adsorption on m-$ZrO_2(\bar{1}11)$.[70] At the interface, water dissociation takes place across the interface; the OH species stays on the Zr top site, that is the preferred water adsorption site, while the H atom transfers to a Rh hollow site close to metal-oxide interface. The O–H bond length at the transition state is 1.41 Å. The reaction is exothermic by −0.11 eV and has a barrier of 0.35 eV. These results show that both pure zirconia and the interface are capable of providing adsorbed OH and H for the subsequent reaction steps, while water activation is much more energetically costly on rhodium, and thus less likely. Altogether, our results provide further support for the experimental observation that the role of the ZrO_2 support is to activate water during WGS.[11–13,28]

Complete water dissociation is a possible source of atomic oxygen for the surface redox reaction pathway. The reaction is endothermic on both m-$ZrO_2(\bar{1}11)$ and at the interface, with an activation energy of 1.34 and 1.00 eV, respectively. On Rh(111), the reaction is exothermic by −0.28 eV and has an activation energy of 0.85 eV. Alternatively, O atoms can also be generated on a catalyst surface by the disproportionation reaction between two OH species, where one OH species donates a proton to the other, forming atomic oxygen and water. On the Rh(111) surface, the reaction is mildly exothermic by −0.19 eV and occurs spontaneously. It has been previously shown that the disproportionation reaction proceeds spontaneously also on the extended Pt(111) surface and at the Ni/Al_2O_3-interface.[18,32] On zirconia, no stable configuration for coadsorbed atomic oxygen and molecular water could be found, but atomic structure relaxation lead to the spontaneous formation of two adsorbed OH species instead, which indicates that disproportination is unlikely on bare ZrO_2. At the interface, molecular water and atomic oxygen are stable when placed far away from each other, but spontaneously form two OH groups when brought close together, making disproportination unfeasible also at the interface.

CO adsorption and oxidation

CO adsorption is exothermic on all three model systems, and the molecule adsorbs linearly through its carbon atom. The most exothermic adsorption energy is on a top site of Rh(111), being −1.91 eV, with also the shortest Rh–C bond length of 1.82 Å. At the interface, the CO prefers adsorption atop interfacial Rh with slightly less exothermic adsorption energy of −1.51 eV, and longer Rh–C bond length of 1.84 Å. On zirconia, CO adsorbs on a Zr top site with a Zr–C bond length of 2.60 Å, and is substantially weaker, only −0.38 eV, which is slightly less exothermic than reported in literature.[39]

As discussed above, atomic oxygen may be obtained from disproportionation or complete water dissociation. Its adsorption energy with respect to gas-phase water is +0.19 eV and +0.31 eV for the interface and rhodium systems, respectively. Prior to CO oxidation, coad-

sorption of CO + O takes place. At the interface, the O atom occupies a Rh-Zr bridge site but moves towards a Zr cation upon CO adsorption on a Rh-top site and the configuration is destabilized by 0.41 eV compared to the infinitely separated species. On rhodium, the CO and O favor adjacent top and hollow sites and the coadsorption structure is destabilized by only 0.08 eV. In the case of the zirconia surface, completely dissociated water has an adsorption energy of −0.03 eV with respect to the water molecule in gas phase and coadsorption with CO is mildly stabilized by −0.13 eV. In the coadsorbed configuration, CO is slightly tilted with the carbon atom closer to the oxygen atom, while the oxygen atom has migrated from the original hollow site to the Zr-Zr bridge site adjacent to CO. Figure 3 illustrates the potential energy surface for CO oxidation by atomic oxygen on Rh, ZrO_2, and the Rh/ZrO_2-interface. On Rh(111), CO oxidation is clearly endothermic by +0.79 eV and

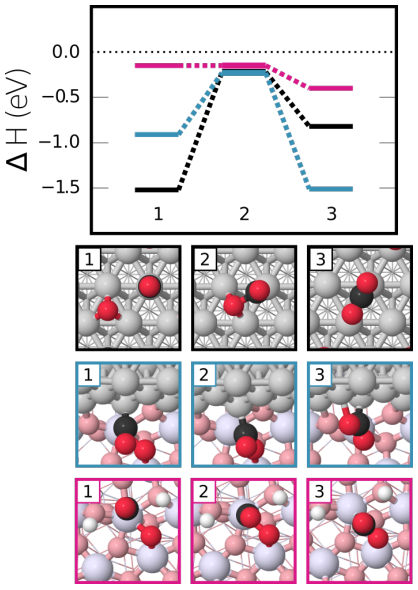

Figure 3: Potential energy diagram and adsorption structures for CO oxidation on Rh, ZrO_2, and the Rh/ZrO_2-interface shown in black, pink, and teal, respectively. In the cases of Rh and the interface, the gas-phase reference is (H_2O - H_2 + CO), but for ZrO_2 it is (H_2O + CO), since hydrogen is kept coadsorbed on the surface. Rh, Zr, H, O_{ads} and O_{lat} atoms are shown in grey, lavender, white, red, and pink, respectively.

has an activation energy of 1.30 eV. At the interface, the reaction is −0.59 eV exothermic due to the weaker binding of reactants and the strong stabilization of CO_2. The activation energy is 0.69 eV, almost half of the barrier on the Rh-surface. CO oxidation is kinetically

most favorable on the zirconia, since the reaction takes place without a kinetic barrier and is exothermic by −0.25 eV. However, the difficulty of forming atomic oxygen on zirconia due to the high barrier of full water dissociation and OH disproportionation renders CO oxidation highly unlikely. The TS geometries on Rh(111) and the interface are both "L-shaped" with C–O bond lengths of 1.81 Å and 1.80 Å, respectively. The TS at the interface resembles the final state of the reaction, while on Rh(111) the TS is more similar to the initial structure.

Besides the difference in activation energies, the strength of CO_2 adsorption varies on the three surfaces; the molecule adsorbs exothermally at the interface and on pure zirconia by −0.68eV and −0.57eV, respectively, but is only weakly physisorbed on the Rh(111) by −0.01eV. This implies that once formed, the CO_2 molecule is likely to desorb immediately from the rhodium surface to the gas-phase, whereas on the zirconia and at the interface, it is available to react further with some other surface species like hydrogen.

Carboxyl formation and dissociation

Carboxyl is formed from coadsorbed OH and CO, and can have either a *cis* or *trans* geometry, the latter isomer being the more stable on all three model systems. The hydrogen atom in *trans*-carboxyl points towards the surface, and the carboxyl can dissociate directly into coadsorbed H and CO_2 by the cleavage of the O–H bond. The PES for the two step process is presented in Figure 4. At the interface and ZrO_2, the carboxyl formation step is endothermic by +0.63 eV and +0.29 eV with a barrier of 0.66 eV and 0.44 eV, respectively. The TS geometries are similar, but the forming C–O bond length is 1.52 Å on zirconia, whereas at the interface the corresponding bond is longer, being 1.74 Å. In contrast, on rhodium the reaction is exothermic by −0.11 eV and has a barrier of 0.41 eV making the carboxyl formation step most facile on rhodium. The C–O bond in the TS is the longest out of the three, being 1.96 Å, and also resembles the final state more than those on the other two surface models. The differences in the reaction and activation energies are due to the relative stabilities of OH and CO on the three model systems. CO adsorbs most strongly

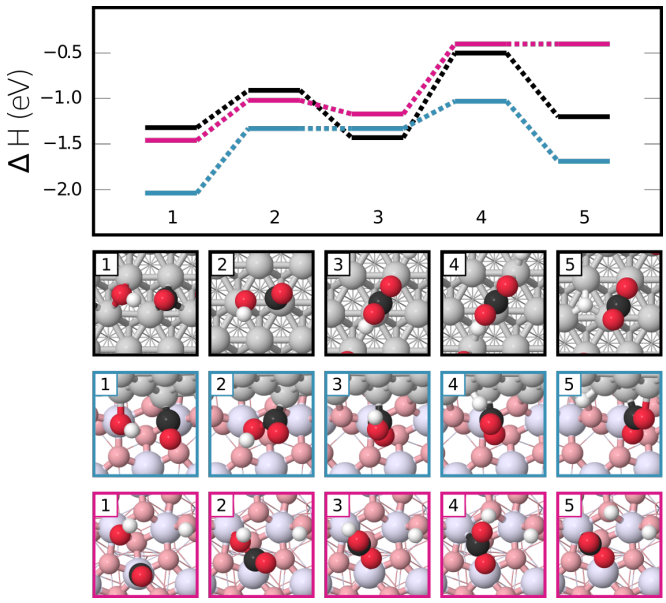

Figure 4: Potential energy diagram and structure geometries for carboxyl formation and dissociation on Rh, ZrO_2, and the interface shown in black, pink, and teal, respectively. In the cases of Rh and the interface, the gas-phase reference is (H_2O - $\frac{1}{2}H_2$ + CO), but for ZrO_2 it is (H_2O + CO), since hydrogen is kept coadsorbed on the surface. Rh, Zr, H, O_{ads} and O_{lat} atoms are shown in grey, lavender, white, red, and pink, respectively.

on the Rh(111), while OH prefers the Zr cation. On pristine Rh and ZrO_2 surfaces, either CO or OH has to adsorb at an unfavorable site. At the interface, both metal and oxide sites are available to accommodate the adsorbates; CO is bound to a Rh atom and OH is bound on a Rh-Zr dual-site, leading to a more stable coadsorbed structure and higher activation energy than for the two pristine surfaces. The carboxyl dissociation step is most feasible at the interface, as it has a barrier of only 0.37 eV, and is exothermic by −0.28 eV. On zirconia and rhodium the reaction is endothermic by +0.76 eV and +0.23 eV, respectively, lacking a kinetic barrier on zirconia, while presenting the largest the dissociation barrier of 0.92 eV on rhodium. Our results for the Rh(111) surface differ from earlier DFT results for the carboxyl pathway.[33,42] This seems to be because we have considered the more stable *trans*-carboxyl as the reaction intermediate, whereas previous studies report results for the *cis*-carboxyl.

Formate formation and dissociation

The discussion of formate formation and dissociation is divided into two parts. First, we compare the pathway on the rhodium and interface, which is followed by the discussion concerning formate formation on bare zirconia. As noted previously by other DFT studies on the WGS,[31,32,51] formate formation in a single step is improbable due to the adsorption geometries of formate, as well as its precursors OH and CO. Instead, CO can react with a hydrogen atom to form a formyl intermediate which can then be oxidized by atomic oxygen into formate. Figure 5 shows the PES of formate formation and dissociation on the Rh(111) surface and at the interface. CO hydrogenation to form a formyl species is endothermic, the reaction energy being +1.17 eV and +0.40 eV on rhodium and the interface, respectively. The corresponding activation energies are 1.44 eV and 0.94 eV, meaning the reaction is kinetically more favorable at the interface. The forming C–H bond is longer at the interface, being 1.35 Å, than on rhodium, being 1.20 Å. Another key difference is that at the interface, hydrogen in bound to an O atom in the initial state and the hydrogenation occurs across the interface. On rhodium, the hydrogen initially occupies a Rh hollow site and in the TS, both CO and H are atop one Rh atom, which leads to a higher activation energy. The next reaction step, oxidation of formyl into formate, is exothermic by −0.68 eV and −1.78 eV and has a barrier of only 0.55 eV and 0.15 eV on rhodium and interface, respectively. Overall the formation of formate is thermodynamically more favorable at the interface than on rhodium, as illustrated in Figure 5. At the interface, formate dissociation into adsorbed CO_2 and atomic hydrogen requires the breaking of a strong O–Zr bond as well as the C–H bond, and has a high barrier of 1.30 eV. On Rh(111), formate is considerably less stable than at the interface, which is reflected in a lower dissociation barrier of 0.85 eV and less endothermic reaction energy. The energetics of the formate route have been previously determined for the Rh(111) surface with DFT.[33] Our reaction energy and barrier for the formyl formation and the reaction energy for formyl oxidation agree with the previous result very well, but our formyl oxidation barrier is ca 0.2 eV lower. Furthermore, we have found a lower barrier for

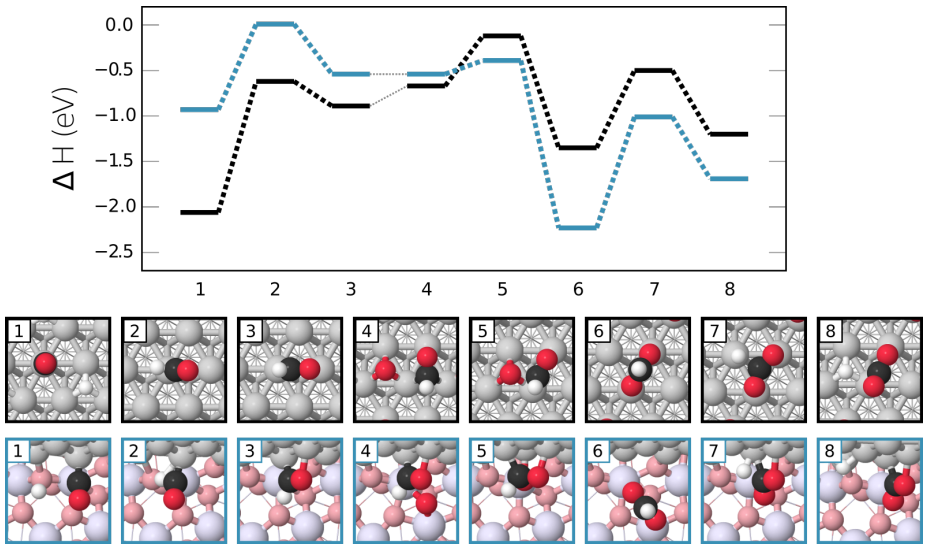

Figure 5: Potential energy diagram and adsorption geometries for formate formation on Rh and the Rh/ZrO_2-interface shown in black, and teal, respectively. For images 1-3, the oxygen atom is treated in a separate computational cell, and the grey line between steps 3 and 4 represents the process of bringing the O atom from infinite separation to the vicinity of the other molecules. The gas-phase reference is (H_2O - $\frac{1}{2}H_2$ + CO). Rh, Zr, H, O_{ads} and O_{lat} atoms are shown in grey, lavender, white, red, and pink, respectively.

the formate dissociation step, 0.85 eV compared to the previous reported value of 1.35 eV.[33] This is due to differences both in the transition state and final state geometries. In our case, formate dissociation is easier than its formation, indicating that the clean metal surface is unable to accumulate formate.

We note that the the reaction between CO_2 and H to form formate has a barrier of 0.68 eV and is exothermic by −0.63 eV at the Rh/ZrO_2-interface. Interestingly, very similar results have been found for the Cu_{38}/m-$ZrO_2(\bar{1}11)$-interface, where formate acts as an intermediate for the CO_2 hydrogenation into methanol.[48] Since we find formate formation to be easier from WGS products than from reactants, it indicates that formate could potentially act as a reaction inhibitor.

Next, we address formate formation on the zirconia surface, where we were unable to locate a good transition state with a competitive activation energy for the formation of the formyl intermediate. The following two pathways were considered. In formyl formation from adsorbed CO and a hydrogen bound to a lattice oxygen, the CO inserts itself into the O–

H bond and forms a "lattice formyl". The transformation of "lattice formyl" to bidentate formates requires extraction of oxygen from the lattice. This is typically costly, since the reduction of zirconia is strongly endothermic if no rhodium atoms or tiny clusters are in the vicinity.[76] In the other reaction pathway, CO reacts with a terminal OH group, again inserting itself into the O–H bond, which leads to a reaction pathway for which the location of transition state fails. One of us has previously investigated a similar reaction pathway, and found that the direct reaction of CO with a terminal OH has an activation energy of at least 1.60 eV.[39] Thus, we suggest the following alternative route for formate formation from WGS products on bare zirconia, as shown in Figure 6. First, adsorbed CO reacts with

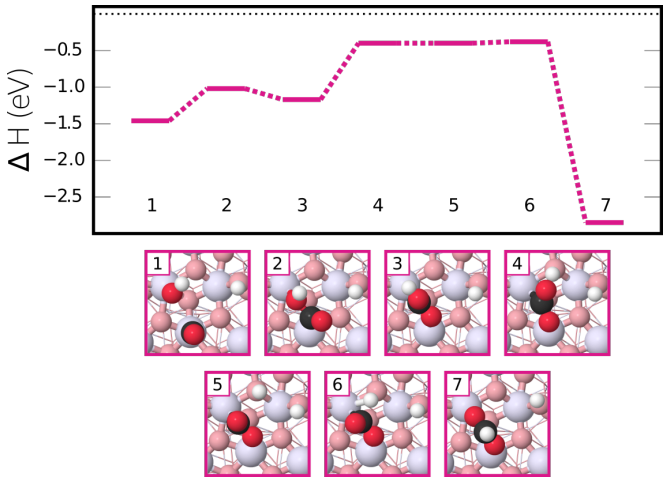

Figure 6: Potential energy diagram and structure geometries for formate formation on ZrO_2. The gas-phase reference is (H_2O + CO). Rh, Zr, H, O_{ads} and O_{lat} atoms are shown in grey, lavender, white, red, and pink, respectively.

a terminal OH to form a carboxyl intermediate, which can then dissociate into adsorbed CO_2 and atomic hydrogen as discussed above. The newly formed CO_2 can either desorb or further react with hydrogen to formate, which is strongly exothermic by −2.45 eV, and has an activation energy of only 0.02 eV. Since CO_2 desorption is endothermic by +0.57 eV, formate formation is preferred. Due to the strong exothermicity of the reaction, formate acts as a thermodynamic "sink", therefore, eventhough CO_2 can also react with hydrogen back to carboxyl and even further back to CO and OH, the equilibrium is shifted towards formate.

Comparison of mechanistic aspects of studied reaction pathways

Based on our DFT results show that water activation is more favorable both on the zirconia support, and at the Rh/ZrO_2-interface, than on Rh(111). This is in line with the previous experimental findings which suggest that the role of the oxide support is to activate water.[11–13,28] Furthermore, the Rh/ZrO_2 interface can provide OH and H species for the subsequent steps of the WGS, thus no diffusion from the bulk oxide to the interface is required. Interstingly, the identity of the metal seems to play a role, since for the Cu/ZrO_2-interface, H_2O dissociation was previously found to be "too facile".[51] This leads to strong adsorption of OH species at the interface and high CO oxidation barriers, rendering the Cu/ZrO_2-interface unreactive.[51]

For the Rh/ZrO_2-interface, all barriers in the carboxyl route are lower than those in the surface redox route, which is limited by the high barrier of full dissociation of water. In particular, the carboxyl formation step which consumes OH, is favored over OH dissociation. Formation of WGS products via the formate intermediate is also unlikely, since it also requires full water dissociation. Furthermore, once formed, formate is very stable, and decomposition to either HCO + O or CO_2 + H requires overcoming a barrier of 1.63 eV or 1.31 eV, respectively. This could lead to the blocking of active sites by formate. As formate can also be formed from CO_2 on the surface, this is a possible source for CO_2 inhibition of the WGS. This has been observed experimentally for the Rh/ZrO_2 catalyst,[22,27] and has been computationally suggested for other systems.[18,31]

On the Rh(111) surface, the highest barrier in the carboxyl pathway is the carboxyl dissociation step, while for the redox reaction the highest barrier is CO oxidation. The activation energy of the carboxyl dissociation step is 0.30 eV lower than that of the CO oxidation step, which means that the associative carboxyl pathway is energetically less costly of the two. Availability of OH groups for carboxyl formation is an important factor for the reaction pathway, as the disproportionation reaction readily consumes OH to form oxygen and water. The formate pathway is unfavorable since the formyl intermediate has a formation

barrier of 1.44 eV, and the equilibrium is towards the backward reaction into CO + H. The rhodium surface is not expected to accumulate formate, since the dissociation barrier is lower than the formation barrier. Because CO_2 only weakly interacts with the metal surface, readsorption of CO_2, and its reaction with hydrogen to formate is unlikely. In addition, the strong binding energy of CO on Rh(111) indicates that the surface will have a high CO coverage, which might lead to self-poisoning and preventing water adsorption.

The zirconia support is not expected to be active for the WGS,[15] although the carboxyl route is shown to be a plausible way to generate the products on the m-$ZrO_2(\bar{1}11)$ surface. One possible reason for the inactivity is that the formation of formate from CO_2 and hydrogen has a very low barrier of only 0.02 eV, and the reaction is strongly exothermic, essentially trapping the products on the surface. The complexity of the network prevents further analysis of the dominant pathway and comparison between the activity of different catalyst domains based on DFT results.

Microkinetic Analysis

To fully elucidate how the pathways discussed above compete under reaction conditions, a comprehensive microkinetic analysis is performed. Microkinetic-reactor model simulations predict consumption of reactants and formation of products as a function of time under given reaction conditions. Herein, we report the results from simulations over three different model systems: a flat Rh(111) surface, a $Rh(111)/ZrO_2(\bar{1}11)$-interface, and an ideal $ZrO_2(\bar{1}11)$ surface. The number of sites in the individual models were estimated to mimic the ratios of the metal, support, and interface sites present in a real catalyst (see SI). For our chosen particle size of 5 nm, the ratio of interface to metal facet sites is 1:12. In the microkinetic analyses temperature was varied from 300 K to 800 K at 100 K intervals and total pressure was set at 2 bar but water to CO ratio was altered. The initial coverage of all intermediates was set to zero for all simulations. No *a priori* assumptions were made about the rate determining step or steady state gas composition and surface coverages. The model

remains thermodynamically consistent through detailed balance. The equilibrium ratio $\frac{K_p}{K_{eq}}$ was evaluated for all simulations at the steady state conditions, and was found to be less than 0.1 in all cases, meaning that the steady state was far from the thermodynamic equilibrium for all simulations. For further details concerning the microkinetic model, please refer to the SI.

WGS on $ZrO_2(\bar{1}11)$

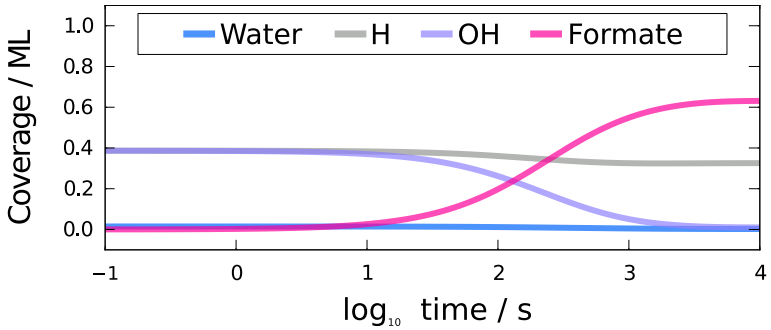

Figure 7: A plot of surface coverages and partial pressures during a microkinetic analysis of the ZrO_2 surface at 700 K with 1:1 H_2O:CO ratio and 2 bar s^{-1} flow rate. For the sake of clarity, intermediates whose coverage was < 0.01 monolayers throughout the entirety of the simulation time were not plotted.

As expected based on experimental results on the bare zirconia,[15] no gas-phase H_2 or CO_2 are produced at any temperature or gas composition studied. At 300 K, the surface is totally covered by molecular water. When the temperature reaches 350 K water dissociation becomes feasible and $\sim$ 5 % of water molecules dissociate, at 500 K already $\sim$ 60 % of water dissociates into OH and H. Formate formation begins at 600 K. Figure 7 shows how formate accumulates on zirconia as a function of time at 700 K. Even at the beginning of the simulation, all molecular water has dissociated and the overall coverage of dissociated water fragments is 0.8 ML. The formate coverage gradually increases reaching 0.6 ML at steady state consuming OH species bound to Zr cations, while the coverage of H atoms attached to lattice oxygens remains virtually unchanged. Once formed, formate species stay on zirconia. The observed consumption of the terminal OH species nicely agrees with

experimental results, where formate formation was found to occur at the expense of terminal OH, while the concentration of "multicoordinated" OH groups remained unchanged.[15] We note that further increase of temperature allows to reach steady state faster but leads to decrease of formate concentration due to fewer terminal OH groups available.

WGS on Rh(111)

On the planar Rh(111) surface, no formation of either product, CO_2 or H_2, was observed independent of reaction conditions and gas ratios studied in microkinetic simulations. This is because the surface is fully occupied by CO molecules with a coverage of 1 ML, which prevents water adsorption. Such a high CO coverage was also observed in microkinetic simulations for the WGS on Al_2O_3 supported Ni nanoparticles.[18] This was attributed to excluding lateral interactions between adsorbates from the model. A high CO coverage was also reported for Pt(111), when lateral interactions were absent.[32] The CO adsorption energy on metal facets is known to be coverage dependent due to the repulsive lateral interactions between the CO molecules.[77] This is also true for rhodium,[78] still, 0.75 ML CO coverage has been reported on rhodium single crystals under ultra high vacuum[79]. To include the coverage dependence of CO adsorption into our model, lateral interactions between CO molecules were taken into account by employing the mean-field approach according to equation 2.0.4 in SI.

Simulations with coverage dependent CO adsorption show that the coverage varies from 0.5 ML to 0.8 ML with temperature ranging from 800 to 300 K, but is independent of the H_2O:CO ratio. Even though there are now free surface sites available for water adsorption and dissociation, no product formation is observed. Our DFT binding energy for water was calculated at 0.25 ML, but a recent DFT study demonstrates that water adsorption energy on metals becomes more exothermic at higher coverage.[73] We hypothesize that weak water adsorption, rather than poisoning of Rh by CO, prevents the WGS reaction from proceeding. To verify this, CO conversion was simulated with 1:1 H_2O:CO ratio and 2 bar s^{-1} flow rate at temperatures from 300 to 800 K at 100 K intervals, with modified H_2O adsorption energies

as seen in Figure 8. The simulations were repeated for two CO adsorption energies: our own DFT value of −1.91 eV and an experimental value of −1.45 eV.[80] All other elementary steps involving water and CO, as well as all activation energies were kept constant at their original DFT values.

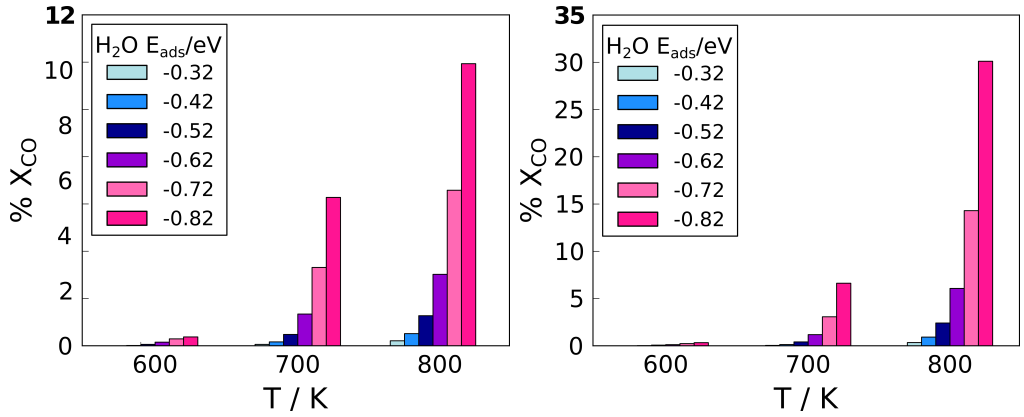

Figure 8: CO conversion,%X_{CO}, as a function of temperature with different water adsorption energies, with the CO adsorption energy of a) −1.91 eV, and b), −1.45 eV, which corresponds to our original DFT computed value, and an experimental value,[80]respectively. The inlet gas composition was kept as 1:1 H_2O:CO with 2 bar s^{-1} flow rate. Note the different ranges of the y-axes.

Figures 8a and 8b show that enhancing water adsorption energy initiates WGS activity in both cases. However, the conversion is lower when the less exothermic experimental value for CO adsorption energy is used. In general, we observe that the water adsorption needs to be modified at least by 0.3 eV to initiate WGS around 700 K, and that CO conversion remains always below 10 % on Rh(111), which is less than half of the conversion at the interface at the same temperature. Only at 800 K with water adsorption energy of −0.82 eV, the CO conversion is slightly higher than at the interface, but due to there being fewer interface sites than Rh(111) sites, the turnover frequency per site is lower at Rh(111). We emphasize that WGS activity on Rh(111) is only achieved by heavily modifying the water adsorption energy, and that if pure DFT values are used, the Rh(111) facet remains inactive for all studied reaction conditions. Since the WGS activity strongly depends on the water adsorption energy, with more exothermic water adsorption leading to higher CO conversion,

we tentatively ascribe the poor WGS activity of Rh(111) to weak water adsorption.

To unravel the reaction mechanism, we use the degree of rate control (DRC) analysis.[72] The summation of the X_{RC} values of all steps in the microkinetic model should equal to unity, meaning that in the case of a single rate determining step, for that step $X_{RC} = 1$. As DRC can only be evaluated when products are formed, we analyzed the reaction mechanism for enhanced H_2O adsorption energy of -0.82 eV, that is 0.5 eV more exothermic than the DFT computed value, but close to the value reported for a high water coverage.[73] This gives a 7 % CO conversion at 700 K, which is substantially lower than at the interface, as shown in the next section. The obtained DRC values are $X_{RC,\,R2} = 0.418$ and $X_{RC,\,R7} = 0.403$ for water dissociation and CO oxidation steps, respectively. These findings show that WGS follows a surface redox mechanism, which is limited by two elementary steps. The negative DRC value of $X_{RC,\,R3} = -0.241$ for the complete water dissociation step indicates that the atomic oxygen needed for CO oxidation must originate from the disproportionation reaction. Interestingly, according to the DFT results, the carboxyl pathway is energetically less costly on Rh(111) than the surface redox reaction. The DRC value for the carboxyl dissociation step is only $X_{RC,\,R10} = 0.129$, which means it is not as rate controlling as the CO oxidation step. The carboxyl formation step has a small negative DRC value, indicating that this step slightly inhibits rate of H_2 production, which in turn means it cannot be part of the dominating pathway. The reason why the carboxyl reaction is unfavorable is likely due to the low availability of OH groups. After formation, the OH groups are immediately consumed by the disproportionation reaction, which is more favorable than COOH formation, due to the more exothermic reaction energy and zero kinetic barrier.

The CO conversion and coverages of the most abundant surface species, CO, O, and H are plotted against H_2O adsorption energy in Figure 9. We observe that CO conversion increases with increasing O coverage, while CO coverage remains constant. As water adsorption becomes more exothermic, partial dissociation becomes more feasible. This in turn provides more OH groups for the disproportionation reaction generating the atomic oxygen

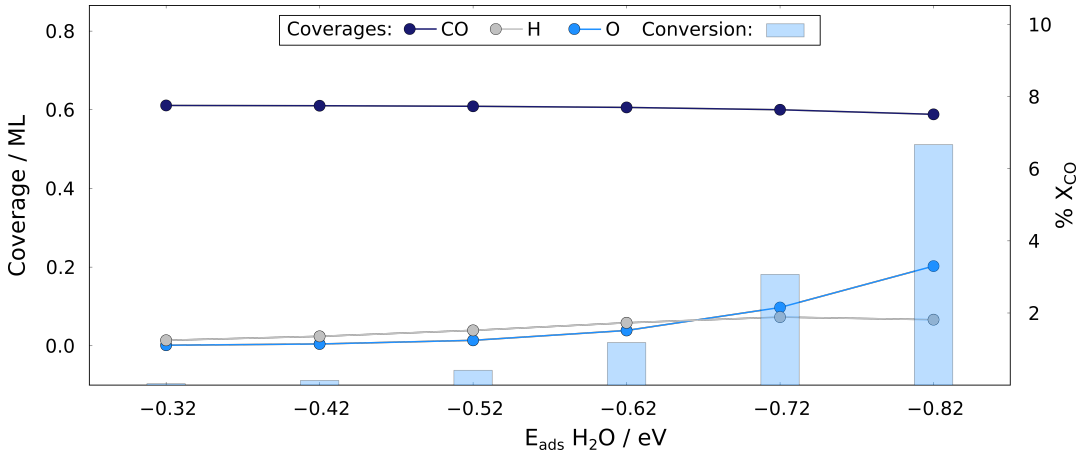

Figure 9: CO, O, and H coverages, and CO conversion, $\%X_{CO}$, at steady state WGS plotted against H_2O adsorption energy. The CO adsorption energy was kept at the original DFT value. Note that the lines connecting the data points are for the purpose of guiding the eye only, and do not indicate interpolation of data. The reaction conditions were kept at 700 K with 1:1 H_2O:CO ratio and 2 bar s^{-1} flow rate.

and leading to higher CO conversion.

WGS at the Rh/ZrO_2-interface

At the Rh/ZrO_2-interface, the production of H_2 and CO_2 begins at 600 K, while at lower temperatures CO and OH are present but do not react further. Since CO binds on the Rh top site at the interface, lateral interactions between CO molecules were treated in the same manner as for Rh(111), but we note that the reaction does proceed even without them. Figure 10 illustrates steady state CO conversion,$\%X_{CO}$, plotted against temperature at differing gas compositions. In general, CO conversion increases with an increasing water:gas ratio, and the maximum conversion, 75%, is reached at 700 K with the ratio 10:1. The simulations demonstrate negligible surface coverage for formate between 300 K and 500 K at all water:gas ratios. However, similar to the zirconia support, formate appears at 600 K and its coverage is ca 0.1 ML at all gas ratios, falling below 0.1 ML at 700 K.

The DRC analysis was perfomed at 700 K with the 1:1 H_2O:CO ratio and 2 bar s^{-1} flow rate. The carboxyl dissociation step was found to be the most rate controlling with $X_{RC,\,R10} = 0.735$. The effect of all the other steps on the overall rate is very small, with the

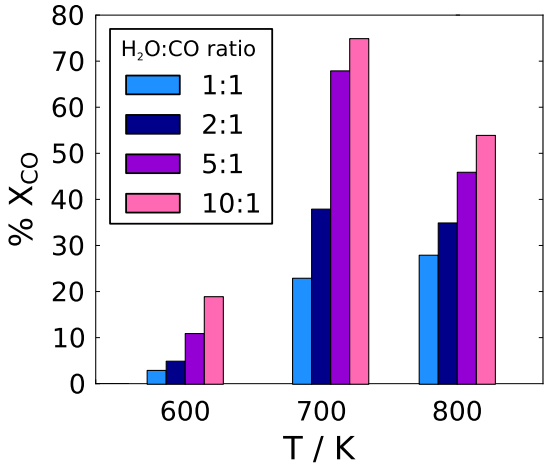

Figure 10: CO conversion, $\%X_{CO}$, at the interface at different reaction conditions.

exception of the formate dissociation step, whose X_{RC} value is 0.151. The formyl oxidation step has a small negative X_{RC} value, meaning that formate formation is slightly inhibitive. Naturally, lowering the dissociation barrier of such a species will have a positive effect on the overall reaction rate. Based on this DRC data, we conclude that at the Rh/ZrO_2-interface the WGS follows the associative reaction mechanism with carboxyl as the reaction intermediate.

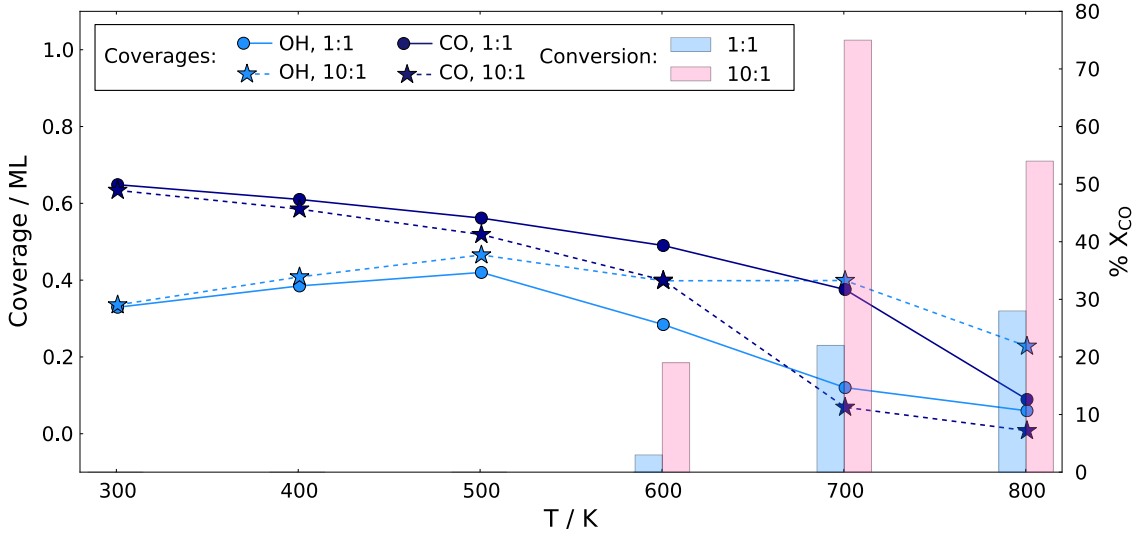

Figure 11: OH and CO coverages, and CO conversion, $\%X_{CO}$, at steady state WGS plotted against temperature under 1:1 and 10:1 H_2O:CO ratio. Note that the lines connecting the data points are for the purpose of guiding the eye only, and do not indicate interpolation of data.

The steady state coverages of OH and CO are plotted against temperature at low and

high water to gas ratio in Figure 11. At both gas compositions, CO coverage decreases with increasing temperature, while OH coverage goes through a maximum and decreases at high temperature. Higher partial pressure of water leads to a higher coverage of OH species, which in turn facilitates higher CO conversion. At 800 K, the conversion is limited by the low coverage of reactants, in particular OH.

Next, we compare the coverages of the most abundant reactive species on the rhodium and interface models. The reaction conditions were selected to be 700 K with 1:1 H_2O:CO ratio and 2 bar s^{-1} flow rate. Moreover, for rhodium a modified H_2O adsorption energy of -0.82 eV was employed. On both models CO coverage is highest among all the species, being 0.6 and 0.4 ML on rhodium and interface, respectively. On rhodium, the second most abundant species is oxygen with a coverage of 0.2 ML, while at the interface oxygen coverage is zero and the second most abundant species is OH with a coverage of 0.3 ML. This difference in the identity and coverage of active surface species further illustrates the difference in the reaction kinetics between the Rh(111) and Rh/ZrO_2-interface.

To shed light on the possible inhibition of the WGS by product gases, we computed the reaction orders with respect to the reactant and product gases (see SI). The reaction order with respect to H_2O is 0.58, while it is only 0.05 with respect to CO. This means that CO partial pressure has a minor effect on the overall reaction rate, while the influence of water partial pressure is substantial. Our result for CO agrees very well with a previous experimental result, while the effect of water partial pressure is overestimated in our study.[22] A similarly over estimated H_2O order was obtained from a WGS microkinetic model on Pt(111).[32] Correctly capturing the negative CO_2 reaction order is typically challenging,[8,40,81] but, in agreement with experiments,[22] we find a negative reaction order for CO_2, our value -0.12 being less negative than the experimental one. In contrast, we also find a negative order with respect to H_2, which was previously experimentally determined to be close to zero.[22] Unfortunately the limited amount of experimental kinetic data makes comparison between the predicted and experimental reaction orders difficult, as the values typically

depend on the reaction conditions, and prevents the use of selective refinement schemes.[8,82,83]

Discussion

Challenges in modeling catalysis at the metal/oxide-interface

In general, construction of computational models for metal/support-interfaces presents a number of challenges for atomistic simulations. One such challenge is the selection of an exchange-correlation functional, which determines the quality of the DFT calculations. It is well-known that approximate exchange-correlation functionals, like GGA, suffer from the self-interaction error, which may lead to inaccuracies in the formation of a metal/oxide-interface, and describing catalytic reactions and charge transfer processes. Typically, the functional is selected based on the comparison of computational and experimental results and the functional that reproduces target experimental values is used for a given chemical process and material. In refinement schemes thermodynamics and kinetics of most important elementary steps are computed at a higher level of theory employing e.g., GGA+U or hybrid functionals.[8,82,83] This allows improved accuracy while minimizing additional computational costs. Furthermore, models are improved until computed and measured quantities agree satisfactorily. The downside is that such an approach is not predictive, whereas in a fully self-consistent, predictive model all elementary steps are computed at the same level of theory. However, there is no *a priori* guarantee that hybrid functionals or the inclusion of +U give better results than GGAs, meta-GGAs, or vdW corrected functionals.[84–86] The reason is that the quality of the underlying GGA, amount of exact-exchange, and the value of the +U parameter all impact reaction and activation energies.[87] In the case of a hybrid functional, the amount of the exact exchange to be included depends on the screening properties of the materials,[88,89] and it is unclear whether universally parametrized (screened) hybrids such as HSE[90,91] or PBE0[92] meet the complexities of metal/oxide-interfaces. These systems might benefit from the use of local hybrids where the amount of exact-exchange depends on the material and local environment[93–95] to capture correct long-range behavior

both in the effectively screened "solid regions" and at the unscreened tail of the "molecular regions". Even if the exact DFT functional is available, the evaluation of free-energies is not easy and may contribute to observed differences between experimental and computational results.[96]

The construction of an atomistic model for the catalyst/support-interface introduces additional complexity. Central questions are whether a small cluster can represent a larger nanoparticle and whether a bulk-like continuous structure – such as a supported rod model – can mimic a nanoparticle perimeter. The choice of an interface model inevitably affects e.g. mechanistic details and computed energies. Care should also be taken in choosing a set of elementary steps to be studied, since too small a subset of reactions considered might lead to incorrect catalytic activity.[82] Finally, the overall catalytic performance needs to be addressed under experimental conditions using first-principles microkinetic modeling or kinetic Monte-Carlo. In kinetic simulations, one should pay attention to how interfacial sites are considered. In the present work, we chose to use a single "interfacial site" while a dual-site model was utilized in a WGS study over MgO-supported metal nanorods.[8] Our choice was based on the atomic-level mechanistic understanding of the Rh/ZrO_2-interface. We observed that once an intermediate adsorbs near the interface, adsorption across the interface becomes unfavorable and therefore there is no need to distinguish between cationic, anionic, and metallic sites at the interface in the microkinetic model. This simplifies the treatment of interfacial coverages and diffusion between different interfacial sites can be neglected.

Computational insights into WGS on zirconia supported rhodium

The present study provides new insight into the reaction mechanism and active domain of the water–gas reaction over the zirconia supported rhodium catalyst. According to our DFT-microkinetic analysis, the interface is the most active domain of the Rh/ZrO_2 catalyst, which is not easily elucidated from DFT results alone because the energy differences between the competing pathways are minor. We predict that the support and bulk rhodium are inactive

for WGS. Only when the interface is explicitly included, product formation is observed. The turn over frequency (TOF) for the reaction at the interface is 38 times greater than the TOF over Rh(111) at identical reaction conditions (700 K with 1:1 H_2O:CO ratio and 2 bar s^{-1} flow rate), even when using the modified H_2O adsorption energy for Rh(111). This implies that while the interface sites make up a minority of the total surface sites, they are still responsible for the majority of the WGS activity. We also note that decreasing particle size leads to a greater number of interfacial sites, and in turn results in greater catalytic activity. Conversely, as metal sintering has been previously identified as a possible deactivation mechanism for WGS over Rh/ZrO_2,[22] this further supports the above interpretation that the interface is the catalytically active domain. Thus, neglecting the oxide-metal interface in computational models might lead to incorrect conclusions on the activity of different catalysts towards WGS. Even if ordering of catalytic activity of different metals can be correctly captured with simplified models, neglecting the metal-support interface even on nominally inert supports may lead to unsatisfactory agreement between computational and experimental results. As observed in this work and previously,[8,9,18,19,51] the interfacial sites can be paramount for the overall catalytic behavior. As such, over-simplified computational models might need refinement to predict correct chemistry and to identify promising bifunctional materials not captured by existing scaling relations.[20,52]

As shown in the present work, and previously experimentally,[15] the zirconia support alone does not catalyze the WGS. Instead the role of the zirconia is to provide dual-sites at the interface. We observe that zirconia forms and accumulates formate, which is not futher converted into products making formate a spectator species, at least when located far away from the interface. It has been previously suggested by experimental studies that metal is needed to dissociate formate.[15,36] According to our DFT calculations, formate is able to diffuse on the zirconia surface at the cost of ca 1 eV which suggests diffusion to the interface is kinetically feasible under WGS conditions, but thermodynamics and site balance favor formate binding on zirconia. The formate dissociation barrier into the WGS products is

1.30 eV at the interface, which is higher than any barrier in the carboxyl pathway, suggesting that the formate mediated pathway would be slower if present, and hinder the overall reaction by taking up active sites. Furthermore, this interpretation seems to be in line with the experimental observations made for Pt/ZrO_2.[36] That study finds that the exchange time of formate was slower than the overall reaction rate, and concluded that formates found on the zirconia support were not involved in the major WGS pathway.

In previous DFT-microkinetic studies, the WGS has been shown to occur via the carboxyl pathway on Pt(111),[32] Cu(111),[31], Au/MgO-interface,[8] and the Cu/ZrO_2-interface.[51] The carboxyl mechanism was also found to be dominant for Rh/α-Al_2O_3 in a study that employed a semi-empirical DFT refined microkinetic model.[83] Our DRC analysis performed here shows that the rate determining step is carboxyl dissociation, same as for Pt(111).[32] Since water activation is easily achieved at the Rh/ZrO_2-interface, it is not a rate controlling step. Similar facile water activation is reported for the Au/MgO-interface, where the carboxyl formation step is the RDS. Although at first glance Cu/ZrO_2 seems similar to our Rh/ZrO_2, partial water dissociation is the rate determining step at the copper-zirconia interface, similar to the bare Cu(111) surface. It was also found that the underlying zirconia support speeds up water dissociation, but the reaction takes place on Cu sites only, whereas we have the water activation taking place on the Rh-Zr dual-sites across the interface. This difference could be due to the interface model used as well as the identity of the metal.

Finally, we compare computed CO conversion to a previously reported experimental value. Our value for CO conversion is ca 40 % at 700 K with 2:1 water:gas ratio, which agrees fortuitously well with the values of $45 - 50$ % reported in literature for similar reaction conditions.[22] Although our model excludes the methanation reaction, this is expected to increase the CO conversion by less than 1 % for the conditions and gas compositions considered.[22] We note that higher content of WGS products in the inlet gas substantially enhances the methane yield.[7] The slightly lower CO conversion compared to the measured value could be due to approximations and models employed in calculations, but also due to

the differences in reaction conditions, catalyst structure, and reactor model.

Conclusions

The first-principles microkinetic model presented herein shows how the water–gas shift (WGS) reaction proceeds over a ZrO_2-supported Rh catalyst. We find that the metal-support interface is the most active domain of the Rh/ZrO_2 system giving highest CO conversion to hydrogen and carbon dioxide. The reaction proceeds along the associative reaction mechanism via a carboxyl intermediate. Interestingly, the carboxyl coverage remains negligible under all reaction conditions and gas ratios studied since it reacts onward immediately, explaining why carboxyl isn't readily observed in experiments.

DFT-computed CO adsorption energy on Rh(111), representing the facets of Rh nanoparticles, leads to 1 ML CO coverage in the microkinetic analysis and renders the surface unable to run the reaction. Including mean-field lateral interactions between CO molecules reduces CO coverage but does not initiate WGS reaction, which is only achieved if the exothermicity of water adsorption is enhanced. In contrast to the interface, the reaction proceeds now via the surface redox route with water activation and CO oxidation as the rate controlling steps. However, even with this modified water adsorption energy, the CO conversion on Rh(111) remains much lower than that achieved at the interface.

The exposure of m-$ZrO_2(\bar{1}11)$ to reactant gases leads to the formation and accumulation of formate from 600 K onwards in microkinetic simulations. Formate on the bulk zirconia is shown to act as a spectator species. Calculations show that formate diffusion to the metal-support interface and its subsequent decomposition are feasible. Even so, the rate of reaction for this process is expected to be slow, and therefore it provides only a minor contribution towards the WGS products, as compared to the carboxyl pathway at the interface.

Our computational study provides an atomically refined model of WGS on zirconia supported rhodium nanoparticles. We show that different parts of the system have distinctly

different roles in the reaction. Although the bulk oxide support and metal particles do not directly take part in the WGS reaction, it is fair to say that they both have a major effect on the reaction mechanism through the formation of the metal-oxide interface. Based on the obtained atomistic information from the combined DFT and microkinetic model, surface coverages and CO conversions were calculated and related to the elementary steps. The obtained results explain and resolve experimental observations and interpretations related to the formation and role of formate as well as the absence of carboxyl. This was achieved by including the support, the metal catalyst, and the interface within the computational model. The present DFT and microkinetic study further strengthens the argument that design of bifunctional catalysts must not rely on simplified models for activity and selectivity as this can potentially lead to the exclusion of prominent material combinations and inaccurate designing principles for a multitude of catalytic reactions.

Supporting Information Available

Full description of microkinetic model and kinetic calculations. List of imaginary frequencies.

Acknowledgement

The work was funded by the Academy of Finland (https://www.aka.fi/en/, grants 277222 (MK, AB, HK) and 307853 (MM)) and University of Jyväskylä. The electronic structure calculations were made possible by the computational resources provided by the CSC — IT Center for Science, Espoo, Finland (https://www.csc.fi/en/). The authors thank Prof. Leon Lefferts and Dr Yingnan Zhao for fruitful discussions.

References

(1) Ratnasamy, C.; Wagner, J. P. Water Gas Shift Catalysis. *Cataly. Rev.* **2009**, *51*, 325–440.

(2) Palo, D. R.; Dagle, R. A.; Holladay, J. D. Methanol Steam Reforming for Hydrogen Production. *Chem. Rev.* **2007**, *107*, 3992–4021.

(3) Zhang, J.; Zhong, Z.; Cao, X.-M.; Hu, P.; Sullivan, M. B.; Chen, L. Ethanol Steam Reforming on Rh Catalysts: Theoretical and Experimental Understanding. *ACS Catal.* **2014**, *4*, 448–456.

(4) Jones, G.; Jakobsen, J. G.; Shim, S. S.; Kleis, J.; Andersson, M. P.; Rossmeisl, J.; Abild-Pedersen, F.; Bligaard, T.; Helveg, S.; Hinnemann, B.; Rostrup-Nielsen, J. R.; Chorkendorff, I.; Sehested, J.; Nørskov, J. K. First Principles Calculations and Experimental Insight into Methane Steam Reforming over Transition Metal Catalysts. *J. Catal.* **2008**, *259*, 147 – 160.

(5) Miao, B.; Ma, S. S. K.; Wang, X.; Su, H.; Chan, S. H. Catalysis Mechanisms of CO_2 and CO Methanation. *Catal. Sci. Technol.* **2016**, *6*, 4048–4058.

(6) Bukur, B. D.; Todic, B.; Elbashir, N. Role of Water-Gas-Shift Reaction in Fischer-Tropsch Synthesis on Iron Catalysts: a Review. *Catal. Today* **2015**, *275*, 66–75.

(7) Thinon, O.; Diehl, F.; Avenier, P.; Schuurman, Y. Screening of Bifunctional Water-Gas Shift Catalysts. *Catal. Today* **2008**, *137*, 29–35.

(8) Zhao, Z.-J.; Li, Z.; Cui, Y.; Zhu, H.; Schneider, W. F.; Delgass, W. N.; Ribeiro, F.; Greeley, J. Importance of Metal-Oxide Interfaces in Heterogeneous Catalysis: A Combined DFT, Microkinetic, and Experimental Study of Water-Gas Shift on Au/MgO. *J. Catal.* **2017**, *345*, 157 – 169.

(9) Cui, Y.; Li, Z.; Zhao, Z.; Cybulskis, V. J.; Sabnis, K. D.; Han, C. W.; Ortalan, V.; Schneider, W. F.; Greeley, J.; Delgass, W. N.; Ribeiro, F. H. Participation of Interfacial Hydroxyl Groups in the Water-Gas Shift Reaction Over Au/MgO Catalysts. *Catal. Sci. Technol.* **2017**, *7*, 5257–5266.

(10) Jacobs, G.; Graham, U. M.; Chenu, E.; Patterson, P. M.; Dozier, A.; Davis, B. H. Low-Temperature Water–Gas Shift: Impact of Pt Promoter Loading on the Partial Reduction of Ceria and Consequences for Catalyst Design. *J. Catal.* **2005**, *229*, 499 – 512.

(11) Azzam, K.; Babich, I.; Seshan, K.; Lefferts, L. Bifunctional Catalysts for Single-Stage Water–Gas Shift Reaction in Fuel Cell Applications.: Part 1. Effect of the Support on the Reaction Sequence. *J. Catal.* **2007**, *251*, 153 – 162.

(12) Grenoble, D.; Estadt, M.; Ollis, D. The Chemistry and Catalysis of the Water Gas Shift Reaction: 1. The Kinetics Over Supported Metal Catalysts. *J. Catal.* **1981**, *67*, 90 – 102.

(13) Panagiotopoulou, P.; Kondarides, D. I. Effect of the Nature of the Support on the Catalytic Performance of Noble Metal Catalysts for the Water–Gas Shift Reaction. *Catal. Today* **2006**, *112*, 49 – 52.

(14) Shekhar, M.; Wang, J.; Lee, W.-S.; Williams, W. D.; Kim, S. M.; Stach, E. A.; Miller, J. T.; Delgass, W. N.; Ribeiro, F. H. Size and Support Effects for the Water–Gas Shift Catalysis over Gold Nanoparticles Supported on Model Al_2O_3 and TiO_2. *J. Am. Chem. Soc.* **2012**, *134*, 4700–4708.

(15) Graf, P.; de Vlieger, D.; Mojet, B.; Lefferts, L. New Insights in Reactivity of Hydroxyl Groups in Water Gas Shift Reaction on Pt/ZrO_2. *J. Catal.* **2009**, *262*, 181 – 187.

(16) Rodríguez, J. A.; Evans, J.; Graciani, J.; Park, J.-B.; Liu, P.; Hrbek, J.; Sanz, J. F.

High Water-Gas Shift Activity in TiO_2(110) Supported Cu and Au Nanoparticles: Role of the Oxide and Metal Particle Size. *J. Phys. Chem. C* **2009**, *113*, 7364–7370.

(17) Green, I. X.; Tang, W.; Neurock, M.; Yates, J. T. Spectroscopic Observation of Dual Catalytic Sites During Oxidation of CO on a Au/TiO_2 Catalyst. *Science* **2011**, *333*, 736–739.

(18) Foppa, L.; Margossian, T.; Kim, S. M.; Müller, C.; Copéret, C.; Larmier, K.; Comas-Vives, A. Contrasting the Role of Ni/Al_2O_3 Interfaces in Water–Gas Shift and Dry Reforming of Methane. *J. Am. Chem. Soc.* **2017**, *139*, 17128–17139.

(19) Sun, K.; Kohyama, M.; Tanaka, S.; Takeda, S. Reaction Mechanism of the Low-Temperature Water–Gas Shift Reaction on Au/TiO_2 Catalysts. *J. Phys. Chem. C* **2017**, *121*, 12178–12187.

(20) Kumar, G.; Nikolla, E.; Linic, S.; Medlin, J. W.; Janik, M. J. Multicomponent Catalysts: Limitations and Prospects. *ACS Catal.* **2018**, *8*, 3202–3208.

(21) Rodriguez, J. A.; Ma, S.; Liu, P.; Hrbek, J.; Evans, J.; Pérez, M. Activity of CeOx and TiOx Nanoparticles Grown on Au(111) in the Water-Gas Shift Reaction. *Science* **2007**, *318*, 1757–1760.

(22) Hakeem, A. A.; Vásquez, R. S.; Rajendran, J.; Li, M.; Berger, R. J.; Delgado, J. J.; Kapteijn, F.; Makkee, M. The Role of Rhodium in the Mechanism of the Water–Gas Shift over Zirconia Supported Iron Oxide. *J. Catal.* **2014**, *313*, 34 – 45.

(23) Yamaguchi, T. Application of ZrO_2 as a Catalyst and a Catalyst Support. *Catal. Today* **1994**, *20*, 199–218.

(24) Heo, I.; Yoon, D. Y.; Cho, B. K.; Nam, I.-S.; Choung, J. W.; Yoo, S. Activity and Thermal Stability of Rh-Based Catalytic System for an Advanced Modern TWC. *Appl. Catal. B-Environ.* **2012**, *121-122*, 75 – 87.

(25) Cao, Y.; Ran, R.; Wu, X.; Zhao, B.; Weng, D. Improved Activity and Durability of Rh-Based Three-Way Catalyst under Diverse Aging Atmospheres by ZrO_2 Support. *J. Environ. Sci.* **2017**, *52*, 197 – 203.

(26) Campa, M.; Ferraris, G.; Gazzoli, D.; Pettiti, I.; Pietrogiacomi, D. Rhodium Supported on Tetragonal or Monoclinic ZrO_2 as Catalyst for the Partial Oxidation of Methane. *Appl. Catal. B-Environ.* **2013**, *142-143*, 423 – 431.

(27) Hakeem, A. A.; Li, M.; Berger, R. J.; Kapteijn, F.; Makkee, M. Kinetics of the High Temperature Water–Gas Shift over Fe_2O_3/ZrO_2, Rh/ZrO_2 and $Rh/Fe_2O_3/ZrO_2$. *Chem. Eng. J.* **2015**, *263*, 427 – 434.

(28) Bunluesin, T.; Gorte, R.; Graham, G. Studies of the Water-Gas-Shift Reaction on Ceria-Supported Pt, Pd, and Rh: Implications for Oxygen-Storage Properties. *Appl. Catal. B-Environ.* **1998**, *15*, 107 – 114.

(29) Kalamaras, C. M.; Panagiotopoulou, P.; Kondarides, D. I.; Efstathiou, A. M. Kinetic and Mechanistic Studies of the Water–Gas Shift Reaction on Pt/TiO_2 Catalyst. *J. Catal.* **2009**, *264*, 117 – 129.

(30) Syzgantseva, O. A.; Calatayud, M.; Minot, C. Revealing the Surface Reactivity of Zirconia by Periodic DFT Calculations. *J. Phys. Chem. C* **2012**, *116*, 6636–6644.

(31) Gokhale, A. A.; Dumesic, J. A.; Mavrikakis, M. On the Mechanism of Low-Temperature Water Gas Shift Reaction on Copper. *J. Am. Chem. Soc.* **2008**, *130*, 1402–1414.

(32) Grabow, L. C.; Gokhale, A. A.; Evans, S. T.; Dumesic, J. A.; Mavrikakis, M. Mechanism of the Water Gas Shift Reaction on Pt: First Principles, Experiments, and Microkinetic Modeling. *J. Phys. Chem. C* **2008**, *112*, 4608–4617.

(33) Lin, C.-H.; Chen, C.-L.; Wang, J.-H. Mechanistic Studies of Water–Gas-Shift Reaction on Transition Metals. *J. Phys. Chem. C* **2011**, *115*, 18582–18588.

(34) Tang, Q.-L.; Chen, Z.-X.; He, X. A Theoretical Study of the Water Gas Shift Reaction Mechanism on Cu(111) Model System. *Surf. Sci.* **2009**, *603*, 2138 – 2144.

(35) Vignatti, C.; Avila, M.; Apesteguía, C.; Garetto, T. Catalytic and DRIFTS Study of the WGS Reaction on Pt-Based Catalysts. *Int. J. Hydrogen Energ.* **2010**, *35*, 7302 – 7312.

(36) Tibiletti, D.; Meunier, F.; Goguet, A.; Reid, D.; Burch, R.; Boaro, M.; Vicario, M.; Trovarelli, A. An Investigation of Possible Mechanisms for the Water–Gas Shift Reaction over a ZrO_2-Supported Pt Catalyst. *J. Catal.* **2006**, *244*, 183 – 191.

(37) Sakurai, H.; Akita, T.; Tsubota, S.; Kiuchi, M.; Haruta, M. Low-Temperature Activity of Au/CeO_2 for Water Gas Shift Reaction, and Characterization by ADF-STEM, Temperature-Programmed Reaction, and Pulse Reaction. *Appl. Catal. A-Gen.* **2005**, *291*, 179 – 187.

(38) Shido, T.; Iwasawa, Y. Reactant-Promoted Reaction Mechanism for Water-Gas Shift Reaction on Rh-Doped CeO_2. **1993**, *141*, 71–81.

(39) Kouva, S.; Andersin, J.; Honkala, K.; Lehtonen, J.; Lefferts, L.; Kanervo, J. Water and Carbon Oxides on Monoclinic Zirconia: Experimental and Computational Insights. *Phys. Chem. Chem. Phys.* **2014**, *16*, 20650–20664.

(40) Ovesen, C.; Clausen, B.; Hammershøi, B.; Steffensen, G.; Askgaard, T.; Chorkendorff, I.; Nørskov, J.; Rasmussen, P.; Stoltze, P.; Taylor, P. A Microkinetic Analysis of the Water–Gas Shift Reaction under Industrial Conditions. *J. Catal.* **1996**, *158*, 170 – 180.

(41) Clay, J. P.; Greeley, J. P.; Ribeiro, F. H.; Delgass, W. N.; Schneider, W. F. DFT Comparison of Intrinsic WGS Kinetics Over Pd and Pt. *J. Catal.* **2014**, *320*, 106 – 117.

(42) Huang, S.-C.; Lin, C.-H.; Wang, J.-H. Trends of Water Gas Shift Reaction on Close-Packed Transition Metal Surfaces. *J. Phys. Chem. C* **2010**, *114*, 9826–9834.

(43) Mohsenzadeh, A.; Richards, T.; Bolton, K. DFT Study of the Water Gas Shift Reaction on Ni(111), Ni(100) and Ni(110) Surfaces. *Surf. Sci.* **2016**, *644*, 53 – 63.

(44) Dietz, L.; Piccinin, S.; Maestri, M. Mechanistic Insights into CO_2 Activation via Reverse Water–Gas Shift on Metal Surfaces. *J. Phys. Chem. C* **2015**, *119*, 4959–4966.

(45) Molina, L. M.; Hammer, B. Active Role of Oxide Support during CO Oxidation at Au/MgO. *Phys. Rev. Lett.* **2003**, *90*, 206102.

(46) Ammal, S. C.; Heyden, A. Origin of the Unique Activity of Pt/TiO_2 Catalysts for the Water–Gas Shift Reaction. *J. Catal.* **2013**, *306*, 78 – 90.

(47) Aranifard, S.; Ammal, S. C.; Heyden, A. On the Importance of the Associative Carboxyl Mechanism for the Water-Gas Shift Reaction at Pt/CeO2 Interface Sites. *J. Phys. Chem. C* **2014**, *118*, 6314–6323.

(48) Larmier, K.; Liao, W.-C.; Tada, S.; Lam, E.; Verel, R.; Bansode, A.; Urakawa, A.; Comas-Vives, A.; Copéret, C. CO_2-to-Methanol Hydrogenation on Zirconia-Supported Copper Nanoparticles: Reaction Intermediates and the Role of the Metal–Support Interface. *Angew. Chem. Int. Edit.* **2017**, *56*, 2318–2323.

(49) Suchorski, Y.; Kozlov, S. M.; Bespalov, I.; Datler, M.; Vogel, D.; Budinska, Z.; Neyman, K. M.; Rupprechter, G. The Role of Metal/Oxide Interfaces for Long-Range Metal Particle Activation During CO Oxidation. *Nat. Mat.* **2018**, *17*, 519–522.

(50) Liu, B.; Liu, J.; Li, T.; Zhao, Z.; Gong, X.-Q.; Chen, Y.; Duan, A.; Jiang, G.; Wei, Y. Interfacial Effects of CeO_2-Supported Pd Nanorod in Catalytic CO Oxidation: A Theoretical Study. *J. Phys. Chem. C* **2015**, *119*, 12923–12934.

(51) Tang, Q.-L.; Liu, Z.-P. Identification of the Active Cu Phase in the Water-Gas Shift Reaction over Cu/ZrO_2 from First Principles. *J. Phys. Chem. C* **2010**, *114*, 8423–8430.

(52) Mehta, P.; Greeley, J.; Delgass, W. N.; Schneider, W. F. Adsorption Energy Correlations at the Metal–Support Boundary. *ACS Catal.* **2017**, *7*, 4707–4715.

(53) Honkala, K.; Hellman, A.; Remediakis, I. N.; Logadottir, A.; Carlsson, A.; Dahl, S.; Christensen, C. H.; Nørskov, J. K. Ammonia Synthesis from First-Principles Calculations. *Science* **2005**, *307*, 555–558.

(54) Li, Q.; García-Muelas, R.; López, N. Microkinetics of Alcohol Reforming for H_2 Production from a FAIR Density Functional Theory Database. *Nat. Commun.* **2018**, *9*.

(55) Enkovaara, J.; Rostgaard, C.; Mortensen, J. J.; Chen, J.; Dułak, M.; Ferrighi, L.; Gavnholt, J.; Glinsvad, C.; Haikola, V.; Hansen, H. A.; Kristoffersen, H. H.; Kuisma, M.; Larsen, A. H.; Lehtovaara, L.; Ljungberg, M.; Lopez-Acevedo, O.; Moses, P. G.; Ojanen, J.; Olsen, T.; Petzold, V.; Romero, N. A.; Stausholm-Møller, J.; Strange, M.; Tritsaris, G. A.; Vanin, M.; Walter, M.; Hammer, B.; Häkkinen, H.; Madsen, G. K. H.; Nieminen, R. M.; Nørskov, J. K.; Puska, M.; Rantala, T. T.; Schiøtz, J.; Thygesen, K. S.; Jacobsen, K. W. Electronic Structure Calculations with GPAW: a Real-Space Implementation of the Projector Augmented-Wave Method. *J. Phys. Condens. Matter* **2010**, *22*, 253202.

(56) Mortensen, J. J.; Hansen, L. B.; Jacobsen, K. W. Real-Space Grid Implementation of the Projector Augmented Wave Method. *Phys. Rev. B* **2005**, *71*, 035109.

(57) Larsen, A. H.; Mortensen, J. J.; Blomqvist, J.; Castelli, I. E.; Christensen, R.; Dułak, M.; Friis, J.; Groves, M. N.; Hammer, B.; Hargus, C.; Hermes, E. D.; Jennings, P. C.; Jensen, P. B.; Kermode, J.; Kitchin, J. R.; Kolsbjerg, E. L.; Kubal, J.; Kaasbjerg, K.; Lysgaard, S.; Maronsson, J. B.; Maxson, T.; Olsen, T.; Pastewka, L.; Peterson, A.; Rostgaard, C.; Schiøtz, J.; Schütt, O.; Strange, M.; Thygesen, K. S.;

Vegge, T.; Vilhelmsen, L.; Walter, M.; Zeng, Z.; Jacobsen, K. W. The Atomic Simulation Environment—a Python Library for Working with Atoms. *J. Phys. Condens. Matter* **2017**, *29*, 273002.

(58) Bahn, S. R.; Jacobsen, K. W. An Object-Oriented Scripting Interface to a Legacy Electronic Structure Code. *Comput. Sci. Eng.* **2002**, *4*, 56–66.

(59) Perdew, J. P.; Burke, K.; Ernzerhof, M. Generalized Gradient Approximation Made Simple. *Phys. Rev. Lett.* **1996**, *77*, 3865–3868.

(60) Perdew, J. P.; Burke, K.; Ernzerhof, M. Generalized Gradient Approximation Made Simple. *Phys. Rev. Lett.* **1997**, *78*, 1396–1396.

(61) Blöchl, P. E. Projector Augmented-Wave Method. *Phys. Rev. B* **1994**, *50*, 17953–17979.

(62) Kolsbjerg, E. L.; Groves, M. N.; Hammer, B. An Automated Nudged Elastic Band Method. *J. Chem. Phys.* **2016**, *145*, 094107.

(63) Henkelman, G.; Uberuaga, B. P.; Jónsson, H. A Climbing Image Nudged Elastic Band Method for Finding Saddle Points and Minimum Energy Paths. *J. Chem. Phys.* **2000**, *113*, 9901–9904.

(64) Jónsson, H.; Mills, G.; Jacobsen, K. In *Classical and Quantum Dynamics in Condensed Phase Simulations*; Berne, B. J., Ciccotti, G., Coker, D. F., Eds.; World Scientific, 1998.

(65) Henkelman, G.; Jónsson, H. Improved Tangent Estimate in the Nudged Elastic Band Method for Finding Minimum Energy Paths and Saddle Points. *J. Chem. Phys.* **2000**, *113*, 9978–9985.

(66) Nitzan, A. *Chemical Dynamics in Condendsed Phases: Relaxation, Transfer, and Reactions in Condensed Molecular Systems*; Oxford University Press, 2006.

(67) Kramida, A.; Yu. Ralchenko,; Reader, J.; and NIST ASD Team, NIST Atomic Spectra Database (ver. 5.5.6), [Online]. Available: `https://physics.nist.gov/asd` [2015, April 16]. National Institute of Standards and Technology, Gaithersburg, MD., 2018.

(68) Larsen, A. H.; Vanin, M.; Mortensen, J. J.; Thygesen, K. S.; Jacobsen, K. W. Localized Atomic Basis Set in the Projector Augmented Wave Method. *Phys. Rev. B* **2009**, *80*, 195112.

(69) Christensen, A.; Carter, E. A. First-Principles Study of the Surfaces of Zirconia. *Phys. Rev. B* **1998**, *58*, 8050–8064.

(70) Bazhenov, A. S.; Honkala, K. Understanding Structure and Stability of Monoclinic Zirconia Surfaces from First-Principles Calculations. *Top. Catal.* **2017**, *60*, 382–391.

(71) Korhonen, S. T.; Calatayud, M.; Krause, A. O. I. Structure and Stability of Formates and Carbonates on Monoclinic Zirconia: A Combined Study by Density Functional Theory and Infrared Spectroscopy. *J. Phys. Chem. C* **2008**, *112*, 16096–16102.

(72) Campbell, C. T. The Degree of Rate Control: A Powerful Tool for Catalysis Research. *ACS Catal.* **2017**, *7*, 2770–2779.

(73) Revilla-López, G.; López, N. Correction: A Unified Study for Water Adsorption on Metals: Meaningful Models from Structural Motifs. *Phys. Chem. Chem. Phys.* **2014**, *16*, 22426–22426.

(74) Hodgson, A.; Haq, S. Water Adsorption and the Wetting of Metal Surfaces. *Surf. Sci. Rep.* **2009**, *64*, 381 – 451.

(75) Bazhenov, A. S.; Lefferts, L.; Honkala, K. Adsorption and Activation of Water on Cuboctahedral Rhodium and Platinum Nanoparticles. *J. Phys. Chem. C* **2017**, *121*, 4324–4331.

(76) Bazhenov, A. S.; Kauppinen, M. M.; Honkala, K. DFT Prediction of Enhanced Reducibility of Monoclinic Zirconia upon Rhodium Deposition. *J. Phys. Chem. C* **2018**, *122*, 6774–6778.

(77) Shan, B.; Zhao, Y.; Hyun, J.; Kapur, N.; Nicholas, J. B.; Cho, K. Coverage-Dependent CO Adsorption Energy from First-Principles Calculations. *J. Phys. Chem. C* **2009**, *113*, 6088–6092.

(78) Dulaurent, O.; Chandes, K.; Bouly, C.; Bianchi, D. Heat of Adsorption of Carbon Monoxide on a Pd/Rh Three-Way Catalyst and on a Rh/Al_2O_3 Solid. *J. Catal.* **2000**, *192*, 262 – 272.

(79) Delouise, L. A.; White, E. J.; Winograd, N. Characterization of CO Binding Sites on Rh[111] and Rh[331] Surfaces by XPS and LEED: Comparison to EELS Results. *Surf. Sci.* **1984**, *147*.

(80) Abild-Pedersen, F.; Andersson, M. CO Adsorption Energies on Metals with Correction for High Coordination Adsorption Sites - A Density Functional Study. *Surf. Sci.* **2007**, *601*, 1747 – 1753.

(81) Koryabkina, N.; Phatak, A.; Ruettinger, W.; Farrauto, R.; Ribeiro, F. Determination of Kinetic Parameters for the Water–Gas Shift Reaction on Copper Catalysts Under Realistic Conditions for Fuel Cell Applications. *J. Catal.* **2003**, *217*, 233 – 239.

(82) Maestri, M.; Livio, D.; Beretta, A.; Groppi, G. Hierarchical Refinement of Microkinetic Models: Assessment of the Role of the WGS and r-WGS Pathways in CH4 Partial Oxidation on Rh. *Ind. Eng. Chem. Res.* **2014**, *53*, 10914–10928.

(83) Maestri, M.; Reuter, K. Molecular-Level Understanding of WGS and Reverse WGS Reactions on Rh Through Hierarchical Multiscale Approach. *Chem. Eng. Sci.* **2012**, *74*, 296 – 299.

(84) Mallikarjun Sharada, S.; Bligaard, T.; Luntz, A. C.; Kroes, G.-J.; Norskov, J. K. SBH10: A Benchmark Database of Barrier Heights on Transition Metal Surfaces. *J. Phys. Chem. C* **2017**, *121*, 19807–19815.

(85) Tameh, M. S.; Dearden, A. K.; Huang, C. Accuracy of Density Functional Theory for Predicting Kinetics of Methanol Synthesis from CO and CO2 Hydrogenation on Copper. *J. Phys. Chem. C* **2018**, *122*, 17942–17953.

(86) Wellendorff, J.; Silbaugh, T. L.; Garcia-Pintos, D.; Nørskov, J. K.; Bligaard, T.; Studt, F.; Campbell, C. T. A Benchmark Database for Adsorption Bond Energies to Transition Metal Surfaces and Comparison to Selected DFT Functionals. *Surf. Sci.* **2015**, *640*, 36 – 44, Reactivity Concepts at Surfaces: Coupling Theory with Experiment.

(87) Tripkovic, V.; Hansen, H. A.; Garcia-Lastra, J. M.; Vegge, T. Comparative DFT+U and HSE Study of the Oxygen Evolution Electrocatalysis on Perovskite Oxides. *J. Phys. Chem. C* **2018**, *122*, 1135–1147.

(88) Skone, J. H.; Govoni, M.; Galli, G. Self-Consistent Hybrid Functional for Condensed Systems. *Phys. Rev. B* **2014**, *89*, 195112.

(89) Skone, J. H.; Govoni, M.; Galli, G. Nonempirical Range-Separated Hybrid Functionals for Solids and Molecules. *Phys. Rev. B* **2016**, *93*, 235106.

(90) Heyd, J.; Scuseria, G. E.; Ernzerhof, M. Hybrid Functionals Based on a Screened Coulomb Potential. *J. Chem. Phys.* **2003**, *118*, 8207–8215.

(91) Krukau, A. V.; Vydrov, O. A.; Izmaylov, A. F.; Scuseria, G. E. Influence of the Exchange Screening Parameter on the Performance of Screened Hybrid Functionals. *J. Chem. Phys.* **2006**, *125*, 224106.

(92) Adamo, C.; Barone, V. Toward Reliable Density Functional Methods Without Adjustable Parameters: The PBE0 Model. *J. Chem. Phys.* **1999**, *110*, 6158–6170.

(93) Jaramillo, J.; Scuseria, G. E.; Ernzerhof, M. Local Hybrid Functionals. *J. Chem. Phys.* **2003**, *118*, 1068–1073.

(94) Borlido, P.; Marques, M. A. L.; Botti, S. Local Hybrid Density Functional for Interfaces. *J. Chem. Theory Comput.* **2018**, *14*, 939–947, PMID: 29227686.

(95) Maier, T. M.; Arbuznikov, A. V.; Kaupp, M. Local Hybrid Functionals: Theory, Implementation, and Performance of an Emerging New Tool in Quantum Chemistry and Beyond. *Wiley Interdiscip. Rev. Comput. Mol. Sci* **2018**, e1378.

(96) Bajpai, A.; Mehta, P.; Frey, K.; Lehmer, A. M.; Schneider, W. F. Benchmark First-Principles Calculations of Adsorbate Free Energies. *ACS Catal.* **2018**, *8*, 1945–1954.

Graphical TOC Entry